


## Two-dimensional Weyl metal and second-order topological insulator phases in the modified Kane-Mele model

Xiaokang Dai and Qinjun Chen <sup>\*</sup>*School of Physics and Electronics, Hunan University, Changsha 410082, China*

(Received 25 December 2023; accepted 1 April 2024; published 17 April 2024)

In this paper, we theoretically investigate quantum phase transitions (QPTs) in a modified Kane-Mele (MKM) model with  $C_{2z}$  and mirror symmetries. The phase diagram of the MKM model uncovers, in addition to the  $\mathbb{Z}_2$  topological insulator phase, a second-order topological insulator (SOTI) phase and three distinct inversion-symmetry-breaking two-dimensional Weyl metal ( $\mathcal{P}$ -breaking 2D WM) phases in response to the interplay of the anisotropic nearest-neighbor hopping and Rashba spin-orbit coupling. During the QPTs among these phases, the edges states evolve topologically and manifest as helical edge states, quasiflat localized edge states, and Fermi arc edge states, respectively, in association with the merging and splitting of band-touching points. To achieve second-order topological corner states, we design a rhombus-shaped nanodisk, where two corner states emerge due to a filling anomaly resulting from the fixed Wannier configuration and  $C_{2z}$  symmetry. In this paper, we not only propose an approach to realize the SOTI phase in the MKM model but also establish a platform for investigating the topological properties of the  $\mathcal{P}$ -breaking 2D WM.

DOI: [10.1103/PhysRevB.109.144108](https://doi.org/10.1103/PhysRevB.109.144108)

### I. INTRODUCTION

The Kane-Mele (KM) model, initially developed for graphene, has been instrumental in revealing a category of  $\mathbb{Z}_2$  topological insulators (TIs) [1–5]. These  $\mathbb{Z}_2$  TIs feature robust spin-resolved helical edge states, resistant to non-magnetic perturbations due to time-reversal (TR) invariance [6,7]. In essence,  $\mathbb{Z}_2$  topological invariants demarcate a phase boundary between the TI and a trivial band insulator [2]. For instance, in an anisotropic KM model, Mondal and Basu [8] illustrated that the interplay between the intrinsic spin-orbit coupling (SOC) and anisotropic nearest-neighbor (NN) hopping effects can result in the annihilation of topology, signifying a topological quantum phase transition (QPT) from the  $\mathbb{Z}_2$  TI into a trivial band insulator. However,  $\mathbb{Z}_2$  topological invariants prove inadequate in capturing the topology of higher-order TIs (HOTIs). Such HOTIs exhibit a distinctive set of highly localized corner or hinge states that exist in dimensions two or more lower than the bulk, despite the  $\mathbb{Z}_2$  values appearing trivial in the bulk-surface correspondence [9]. Essentially, the presence of in-gapped corner or hinge states in HOTIs is attributed to the quantization of polarization due to symmetries, adhering to higher-order bulk-boundary correspondences [9–14]. Consequently, it suggests the potential for a topological QPT from  $\mathbb{Z}_2$  TI to HOTI.

Significant research has focused on manipulating the KM model to explore the second-order TI (SOTI) phase [15–19]. An in-plane [15–18] or out-plane [19] Zeeman field is introduced to gap out the helical edge states and creates the so-called boundary-localized mass domains with opposite signs at the adjacent edges. When specific crystal

symmetries are preserved, these manipulations enable the realization of quantized, termination-dependent second-order topological corner states. However, another mechanism to realize the SOTIs involves a strategically designed Wannier configuration protected by  $C_{nz}$  symmetries. In this scenario, a mismatch between the Wannier centers and the bulk atoms induces a filling anomaly along the edges to simultaneously satisfy charge neutrality and the crystal symmetry and consequently giving rise to a quantized fractional charge at the corners [20–22]. Due to the crystal symmetry protection, the quantization of corner states is robust against weak disorder that preserves crystal symmetry globally [20,23–25]. However, when the disorder strength is strong enough to close the bulk band gap, all states become localized, and the HOTI turns into an Anderson insulator according to the delocalization-localization transition [23,26,27].

In this paper, we present an alternative approach to realize a SOTI in the modified KM (MKM) model, adhering to the second mechanism. Whereas the anisotropic NN hopping effect removes the last element of  $C_{nz}$  symmetry—the  $C_{3z}$  symmetry—the band-touching points are no longer confined to the high-symmetry points in the Brillouin zone (BZ), i.e.,  $K$  and  $K'$  in the honeycomb lattice. To induce the filling anomaly, one straightforward method is to restore the  $C_{2z}$  symmetry by completely removing the staggered on-site potential, while the anisotropy NN hopping effect is maintained as a residual effect of the broken  $C_{3z}$  symmetry. Equivalent to the manipulation on the differential hopping between the interunit and intraunit cells, adjusting the anisotropic NN hopping strength forces the Wannier centers to occupy the atomic-unoccupied Wyckoff positions, resulting in the formation of obstructed atomic insulators [28]. Following this consideration, we demonstrate that the SOTI can be achieved in a rhombus-shaped nanodisk. The filling anomaly, induced

<sup>\*</sup>chenqj@hnu.edu.cn

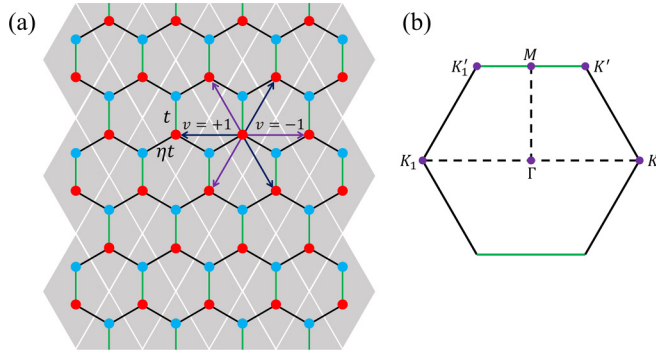


FIG. 1. The modified Kane-Mele (MKM) model with A (red) and B (light blue) sublattices. Anisotropic nearest-neighbor (NN) couplings for interunit and intraunit cells are represented by black and green solid lines, respectively. The signs of next-NN (NNN) couplings  $v_{ij}$  are indicated by dark blue and purple arrows, respectively. (b) The Brillouin zone (BZ) of the MKM model.

by the  $C_{2z}$  symmetry, plays a critical role in the formation of corner-localized states. Moreover, the distinctive topological characteristic of the SOTI is identified through a quantized anisotropic polarization.

On the other hand, as the strength of Rashba SOC (RSOC) increases, the breaking of inversion symmetry removes the fourfold degeneracy at the TR invariant points, transforming the system into a metal phase [29], characterized by double degenerate Weyl points (WPs) with definite chirality, akin to three-dimensional (3D) topological Weyl semimetals [30–33]. Therefore, we identify this metallic phase as an inversion-symmetry-breaking two-dimensional Weyl metal ( $\mathcal{P}$ -breaking 2D WM). Beyond the role played in the KM model, the interplay between anisotropic NN hopping and RSOC can lead to QPTs between topological insulating phases and the 2D WM phases, which topologically link to the evolution of boundary states. Notably, the  $\mathcal{P}$ -breaking 2D WM phase can only transit into a TI phase that preserves TR symmetry, in contrast with the TR-symmetry-breaking 2D WM phase found in ferromagnetic materials, which is known to be the parent of the quantum anomalous Hall insulator phase [34–37].

The rest of the paper is organized as follows. In Sec. II, we first establish a phase diagram for the MKM model with  $C_{2z}$  and mirror symmetries in the parameter space of  $(\eta, \lambda_R/\lambda_{SO})$ , with  $\eta$ ,  $\lambda_R$ , and  $\lambda_{SO}$  being the anisotropic parameter, the strength of RSOC, and the strength of intrinsic SOC, respectively. Subsequently, in Sec. III, we illustrate topological boundary states in the semi-infinite honeycomb configurations, delving into the characteristics of edge states and their evolutions during the topological QPTs. The realization of the corner states of the SOTI phase in a rhombus-shaped nanodisk is illustrated in Sec. IV. Finally, we conclude this paper in Sec. V.

## II. MODEL AND PHASE DIAGRAM

To preserve the  $C_{2z}$  and mirror symmetries, we consider an MKM model on a honeycomb lattice depicted in Fig. 1(a). The tight-binding MKM Hamiltonian in the absence of the

staggered on-site potential is given by [2]

$$H = \sum_{\langle i,j \rangle} t_{ij} c_i^\dagger c_j + i\lambda_{SO} \sum_{\langle\langle i,j \rangle\rangle} v_{ij} c_i^\dagger s_z c_j + i\lambda_R \sum_{\langle i,j \rangle} c_i^\dagger (\mathbf{s} \times \mathbf{d}_{ij})_z c_j. \quad (1)$$

The first term on the right-hand side represents the anisotropic NN coupling. The hopping strength  $t_{ij}$  takes  $t_{ij} = t$  along the armchair (AM) direction (within intraunit cells) and  $t_{ij} = \eta t$  along the zigzag (ZZ) direction (connecting interunit cells), represented by the green and black solid lines in Fig. 1(a), respectively. The strength  $t$  is material dependent, e.g.,  $t \approx 2.8\text{eV}$  in graphene [38], and  $\eta \neq 1$  is the anisotropic parameter introduced to break the  $C_{3z}$  symmetry. Note that, when  $\eta = 1$ , the model reduces to the general KM model [2]. The second term describes the intrinsic next NN (NNN) SOC with strength  $\lambda_{SO}$ . The NNN SOC is crucial in establishing the topological insulating phase, as it opens a bulk gap in the KM model [1]. Here,  $v_{ij} = \pm 1$  corresponds to the clockwise and counterclockwise orientations of the NNN sites, depicted by dark blue and purple arrows in Fig. 1(a), respectively. The last term on the right signifies the NN RSOC with strength  $\lambda_R$ , where  $\mathbf{d}_{ij}$  is the unit vector along the bond where the electron traverses going from site  $j$  to NN site  $i$ . This term breaks the inversion symmetry and can modify the bulk gap by inducing band inversion. The vector  $\mathbf{s} = (s_0, s_x, s_y, s_z)$  consists of the Pauli matrices, representing the electron spin.

After applying the Fourier transformation to Eq. (1), we obtain the Hamiltonian in  $\mathbf{k}$  space [2]:

$$H(\mathbf{k}) = \sum_{a=1}^5 d_a(\mathbf{k}) \Gamma^a + \sum_{a<b=1}^5 d_{ab}(\mathbf{k}) \Gamma^{ab}, \quad (2)$$

with  $\Gamma^a = (\sigma_x \otimes s_0, \sigma_z \otimes s_0, \sigma_y \otimes s_x, \sigma_y \otimes s_y, \sigma_y \otimes s_z)$ ,  $\Gamma^{ab} = [\Gamma^a, \Gamma^b]/(2i)$ , and  $\sigma_j (j = 0, x, y, z)$  being the Pauli matrices that act on the sublattice. The nonzero coefficients  $d_a(\mathbf{k})$  and  $d_{ab}(\mathbf{k})$  are

$$d_1(\mathbf{k}) = \left( t + 2\eta t \cos \frac{1}{2} k_x \cos \frac{\sqrt{3}}{2} k_y \right),$$

$$d_3(\mathbf{k}) = \lambda_R \left( 1 - \cos \frac{1}{2} k_x \cos \frac{\sqrt{3}}{2} k_y \right),$$

$$d_4(\mathbf{k}) = -\sqrt{3} \lambda_R \sin \frac{1}{2} k_x \sin \frac{\sqrt{3}}{2} k_y,$$

$$d_{12}(\mathbf{k}) = -2\eta t \cos \frac{1}{2} k_x \sin \frac{\sqrt{3}}{2} k_y,$$

$$d_{15}(\mathbf{k}) = \lambda_{SO} \left( 2 \sin k_x - 4 \sin \frac{1}{2} k_x \cos \frac{\sqrt{3}}{2} k_y \right),$$

$$d_{23}(\mathbf{k}) = -\lambda_R \cos \frac{1}{2} k_x \sin \frac{\sqrt{3}}{2} k_y,$$

$$d_{24}(\mathbf{k}) = \sqrt{3} \lambda_R \sin \frac{1}{2} k_x \cos \frac{\sqrt{3}}{2} k_y,$$

respectively.

The energy band dispersion of the Hamiltonian in Eq. (2) significantly depends on the parameters  $\eta$ ,  $\lambda_{SO}$ , and  $\lambda_R$ . By varying these parameters, the model can undergo (topological) QPTs among different phases. These QPTs are characterized by the closing or opening of the bulk band gap along certain symmetry-invariant lines. In the current MKM model, mirror symmetries require that, at the phase boundaries where QPTs occur, the bulk band gap must close precisely at the mirror-invariant lines [39], namely, the  $M_x$ -invariant lines  $\Gamma$ - $K$  and  $M$ - $K'$ , as well as the  $M_y$ -invariant line  $\Gamma$ - $M$ . Therefore, our analysis will focus on exploring how the energy bands along these mirror-invariant lines are affected by the parameters.

Along the  $M_x$ -invariant lines  $\Gamma$ - $K$  and  $M$ - $K'$ , the energy band dispersion relations, can be expressed in a compact form:

$$E_{\gamma_1, \gamma_2}(k_x, k_y) = \gamma_2 d_{24}(\mathbf{k}) + \gamma_1 \sqrt{d_1^2(\mathbf{k}) + [d_{15}(\mathbf{k}) - \gamma_2 d_3(\mathbf{k})]^2}, \quad (3)$$

where  $\gamma_1 = +1(-1)$  denotes the conduction (valence) band,  $\gamma_2 = \pm 1$  is the subband index, and  $j = 1, 2$  correspond to the symmetry-invariant lines  $\Gamma$ - $K$  and  $M$ - $K'$ , respectively. When the valence and the conduction bands touch at a critical point  $(k_{xC}, k_{yC})$ , the following condition must be fulfilled:

$$E_{-,+}(k_{xC}, 0) = E_{+,-}(k_{xC}, 0), \quad (4)$$

for  $j = 1$ , and

$$E_{+,+}\left(k_{xC}, \frac{2\sqrt{3}\pi}{3}\right) = E_{-,+}\left(k_{xC}, \frac{2\sqrt{3}\pi}{3}\right), \quad (5)$$

for  $j = 2$ , respectively. By solving Eqs. (4) and (5), we can determine two phase boundaries, which are expressed as functions of  $\lambda_R$  in terms of  $\eta$  and  $\lambda_{SO}$ :

$$\lambda_R^2 = \left[ \frac{12\lambda_{SO}^2(1+2\eta)^2}{(2+\eta)^2} - \frac{4t^2(1+2\eta)(\eta^3+3\eta^2-4)}{9(2+\eta)^2} \right] \times \Theta\left(\eta + \frac{1}{2}\right)\Theta(1-\eta), \quad (6)$$

for  $j = 1$ , and

$$\lambda_R = 4\lambda_{SO} \sqrt{1 - \frac{1}{4\eta^2} \Theta(1-\eta) \Theta\left(\eta - \frac{1}{2}\right)}, \quad (7)$$

for  $j = 2$ , respectively. The solutions also yield information about the locations of the band-touching points:  $\cos \frac{1}{2}k_{xC} = \frac{1-4\eta}{2(2+\eta)}$  for  $j = 1$ , and  $\cos \frac{1}{2}k_{xC} = \frac{1}{2\eta}$  for  $j = 2$ . Notably, the locations of these band-touching points depend solely on  $\eta$ , a characteristic like that found in the modified Haldane model [40].

On the other hand, the energy dispersion taken along the  $M_y$ -invariant line  $\Gamma$ - $M$  can be expressed in the following form:

$$E_{\gamma_1, \gamma_2}(0, k_y) = \gamma_1 \sqrt{[d_1(\mathbf{k}) + \gamma_2 d_{23}(\mathbf{k})]^2 + [d_{12}(\mathbf{k}) + \gamma_2 d_3(\mathbf{k})]^2}. \quad (8)$$

At the critical band-touching points  $(0, k_{yC})$ , Eq. (8) implies the condition:  $E_{-,+}(0, k_{yC}) = E_{+,+}(0, k_{yC})$ . Solving this condition yields another phase boundary:

$$\eta = 0.5, \quad (9)$$

and the information of the location of band-touching point:  $\cos \frac{\sqrt{3}}{2}k_{yC} = \frac{\lambda_R^2 - 1}{\lambda_R^2 + 1}$ . The location of the band-touching point moves from  $\bar{M}(\lambda_R = 0)$  to  $\Gamma(\lambda_R = \infty)$  with increasing  $\lambda_R$  along the phase boundary of Eq. (9), implying that the gap-closing bulk state remains robust against RSOC if  $\eta = 0.5$ .

The RSOC, typically introduced by applying a perpendicular external field [41] or induced by substrate effects [42], leads to the breaking of inversion symmetry. As a result, the energy bands are no longer Kramers degenerate except at the TR-invariant momenta [39]. Interestingly, computing the winding number along a closed orbit encircling each band-touching point yields zero, indicating nonchirality. This type of neutral degeneracy arises from the merging of two WPs with opposite charges [43] and has been predicted in 3D optical crystals [44,45] and on a 2D square lattice [46]. Therefore, when the inversion symmetry is broken, the phase boundaries with nonvanishing  $\lambda_R$  as defined by Eqs. (6), (7), and (9) indicate the emergence of twofold-degenerate neutral band-touching points. However, when  $\lambda_R$  vanishes, the inversion symmetry is retained, and both the conduction and valence bands are twofold degenerate, leading to fourfold degenerate neutral band-touching points at phase boundaries.

Plotting the boundaries with Eqs. (6), (7), and (9), we can construct a 2D phase diagram in the parameter space of  $(\eta, \lambda_R/\lambda_{SO})$ , as shown in Fig. 2(a). For the illustrative case, we set  $\lambda_{SO} = 0.06t$  [2,8]. We focus on the upper half plane ( $\lambda_R \geq 0$ ) since the phase diagram is symmetric about  $\lambda_R = 0$ . The boundaries delineated by Eqs. (6), (7), and (9) are represented by blue, red, and gray solid lines, respectively. As a result, the phase diagram is divided into five distinct phase zones, colored in light yellow, light magenta, light blue, light green, and light orange. Notably, there are two triple points located at  $T_1(1, 2\sqrt{3})$  and  $T_2(0.5, 0)$  and a quadruple point at  $Q(0.5, 11.45)$  on the upper half plane. In Figs. 2(c)–2(g), the maps of the bulk energy gap are plotted with parameters selected from each phase zone. Correspondingly, one can distinguish that the light yellow and light magenta zones represent insulating phases, while the light blue, light green, and light orange zones are in metallic phase.

To further distinguish the phases associated with the topological features, we start with the triple point  $T_1(1, 2\sqrt{3})$ , which hosts neutral degeneracies at the corners of the first BZ [as shown in Fig. 2(b)]. This point is generally regarded as the critical condition for the QPT between the  $\mathbb{Z}_2$  TI phase and the metal phase in the KM model. Following Kane and Mele's argument [1], we identify the light magenta zone, enclosed by the blue boundary [Eq. (7)] and  $\eta = 1$ , as the  $\mathbb{Z}_2$  TI phase. This phase is characterized by a nontrivial topological invariant  $\mathbb{Z}_2 = 1$  [2]. In the  $\mathbb{Z}_2$  TI phase zone, the interplay between  $\eta$  and  $\lambda_R/\lambda_{SO}$  does not destroy the bulk-edge topology until the two parameters reach the blue boundary, where  $\lambda_R/\lambda_{SO}$  becomes a function of  $\eta$ , as shown in Eq. (7). In other words, unless the RSOC is sufficiently strong to close the band gap induced by intrinsic SOC, the band topology remains unchanged. This is consistent with the realization of the TI phase in the KM model by employing a small  $\lambda_R/\lambda_{SO}$  [1]. However, when RSOC is turned off, the  $\mathbb{Z}_2$  TI is allowed to transition to another insulating phase (for  $\eta < 0.5$ ) by crossing the other triple point  $T_2(0.5, 0)$ . Although the  $\mathbb{Z}_2$  analysis suggests a

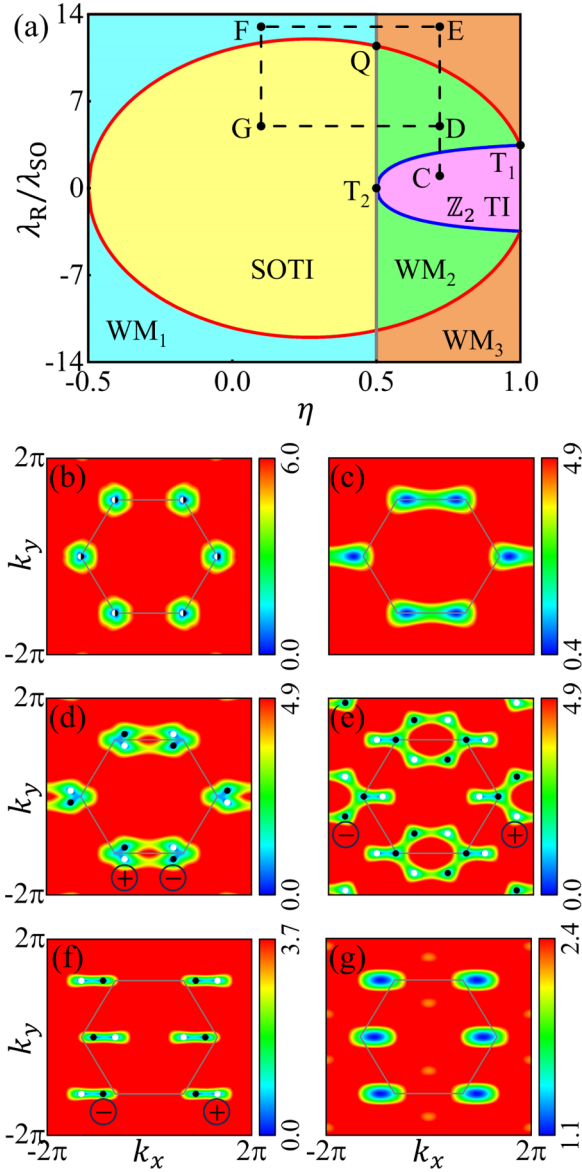


FIG. 2. (a) Phase diagram of the modified Kane-Mele (MKM) model in the parameter space  $(\eta, \lambda_R/\lambda_{SO})$ . The phase boundaries determined by Eqs. (6), (7), and (9) are marked with red, blue, and gray solid lines, respectively. Light yellow and light magenta zones indicate the second-order topological insulator (SOTI) and  $\mathbb{Z}_2$  TI phases, respectively. Three distinct Weyl metal (WM) phases are represented in light blue, light green, and light orange. (b) and (c)–(g) represent energy gap map for points  $T_1$  and C–G, marked by black solid circles in the phase diagram. Black solid circles, white solid circles, and half white and half black circles denote WPs with negative chirality, positive chirality, and neutrality, respectively.

trivial phase, we will show in Sec. IV that this insulating phase can be manipulated into a SOTI phase that is characterized by the nonzero anisotropic polarization and the emergence of corner states.

In the KM model with  $\lambda_R/\lambda_{SO} > 2\sqrt{3}$ , corresponding to the parameter path above the triple point  $T_1$  along  $\eta = 1$ , Du *et al.* [29] demonstrated the emergence of additional band-touching points around  $K$  and  $K'$ . In our MKM model, RSOC

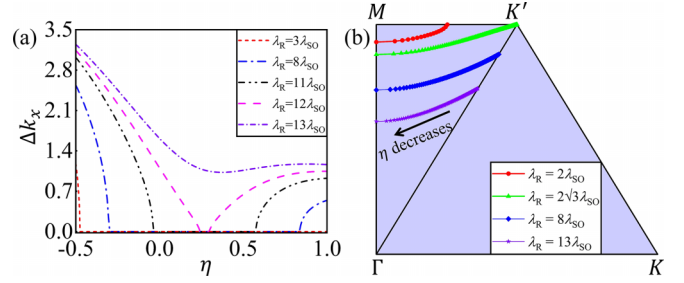


FIG. 3. (a) Variation of the distance between two  $W_1$ 's as a function of  $\eta$  for different  $\lambda_R$  values. (b) Trajectory of  $W_2$  within the first Brillouin zone (BZ) as  $\eta$  varies, depicted for cases where  $\lambda_R < 2\sqrt{3}\lambda_{SO}$  (red) and  $\lambda_R > 2\sqrt{3}\lambda_{SO}$  (blue and purple). The black arrow represents the direction of decreasing  $\eta$ .

influences these band-touching points in a manner akin to the KM model. Moreover, the introduction of anisotropic NN hopping causes the band-touching points to deviate the  $C_{3z}$ -invariant points/lines, owing to the breaking of  $C_{3z}$  symmetry. Furthermore, as a result of the constraint of mirror symmetry, two kinds of band-touching points are found in the MKM model: one type (referred to as  $W_1$ ) of band-touching points locates at the mirror-symmetry line  $K_1$ - $\Gamma$ - $K$ ; while the other type (referred to as  $W_2$ ) is fully unpinned. At the phase boundaries separating insulating and metallic phases, the band-touching points are nonchiral and share the same Fermi energy, implying a semimetal phase. As parameters continue to evolve, each neutral band-touching point splits into two copies with opposite chirality. Moreover, the stronger RSOC further distorts the particle-hole symmetry, leading to a misalignment of the band-touching points at the Fermi energy. Therefore, the system undergoes a QPT into a nontrivial metallic phase. In Figs. 2(d)–2(f), we highlight the signs of the winding numbers of the band-touching points by black and white solid circles. These points exhibit characteristics like 3D WPs, often described as *monopoles* characterized by a chirality that signifies the topological charge [30–33]. Due to TR symmetry, each crossing point at  $\mathbf{k}$  is associated with a TR partner at  $-\mathbf{k}$  with the same chirality [47]. According to the no-go theorem, which claims that the total topological charge within the first BZ must be zero [48], the emergence of band-touching points must be even-numbered pairs. As illustrated in Figs. 2(d)–2(f), the number of band-touching points is either two pairs [in the cases of Figs. 2(d) and 2(f)] or four pairs [in the case of Fig. 2(e)]. These results suggest that the twofold-degenerate band-touching points from the split of neutral degeneracy in the MKM model can be considered 2D analogs of  $\mathcal{P}$ -breaking WPs. Consequently, we attribute these metallic phases as the  $\mathcal{P}$ -breaking 2D WM phases.

The 2D WMs can be classified into three distinct types:  $WM_1$ ,  $WM_2$ , and  $WM_3$ . This classification is based on the number and distribution of resident WPs, as indicated in the corresponding phase zones in Fig. 2(a). As shown in Figs. 2(d)–2(e),  $WM_1$  and  $WM_2$  each contain two pairs of WPs, whereas  $WM_3$  hosts four pairs. In  $WM_1$ , two sets of  $W_1$ 's are located along the invariant line  $K_1$ - $\Gamma$ - $K$  due to the mirror and  $C_{2z}$  symmetries. Figure 3(a) illustrates the variation of the relative distance  $\Delta k_x$  between two  $W_1$ 's of opposite



chirality within each pair, as a function of the parameter  $\eta$  for various fixed values of  $\lambda_R$ . It is important to note that, when  $\Delta k_x$  drops to zero, each pair of  $W_1$ 's with opposite chirality annihilates, resulting in a neutral degeneracy. This occurs when the parameter coordinates intersect the red boundary in the phase diagram. Interestingly, the pairwise  $W_1$ 's demonstrate considerable robustness against variations in  $\eta$  at sufficiently large RSOC and are topologically invariant even when  $\eta$  crosses the phase boundary ( $\eta = 0.5$ ) between  $WM_1$  and  $WM_3$ . This implies that there must be two pairs of  $W_1$ 's constituting two of the four pairs of WPs in  $WM_3$ .

In the  $WM_2$  phase, the set of  $W_2$ 's diverges from the mirror-invariant lines and is located at generic  $\mathbf{k}$  points in the interior of the BZ. Figure 3(b) illustrates the trajectories of a typical  $W_2$  in the first quadrant of the BZ, depicted as a function of the parameter  $\eta$  for various fixed  $\lambda_R$ 's. The positions of the remaining three WPs can be inferred by applying the mirror and  $C_{2z}$  symmetries. Unlike the  $W_1$ 's, the  $W_2$ 's are fully unpinned, leading to two possible scenarios for the merging of two  $W_2$ 's with opposite chirality. The merging can occur either on the  $M_x$ -invariant line ( $M-K'$ ) or on the  $M_y$ -invariant line ( $\Gamma-M$ ), depending on whether the parameters align with the blue or gray phase boundary, respectively. In contrast to the  $W_1$ 's, the two pairs of  $W_2$ 's exhibit robustness against variations in  $\lambda_R$ , even when crossing the phase boundary between  $WM_2$  and  $WM_3$ . Hence, the  $W_2$ 's contribute to the other two of the four pairs of WPs in the  $WM_3$ .

Typically, the  $WM_3$  phase can be considered the combination of the  $WM_1$  and  $WM_2$ . Excepting for the quadruple point Q—where the red and gray boundaries intersect—the processes of annihilation and creation of  $W_1$  and  $W_2$  are mutually independent during the QPT between  $WM_3$  and either  $WM_1$  or  $WM_2$ . This independence implies that they cannot be simultaneously annihilated by solely breaking either the inversion symmetry or the  $C_{3z}$  symmetry. According to the bulk-boundary correspondence, these WPs can give rise to Fermi arc edge states in the nanoribbon configurations. As will be demonstrated in the subsequent section, these edge states evolve topologically in association with the merging and splitting of WPs.

### III. EDGE STATES IN THE MKM MODEL

Since edge states are highly sensitive to the details of the Hamiltonian near the edge, we consider two fundamentally different bond-cutting operations within a 2D honeycomb lattice: strong-bond-cutting (SBC) and weak-bond-cutting (WBC). These operations are analogous to the manipulation of endpoints in the Su-Schrieffer-Heeger (SSH) model [49]. Geometrically, each bond-cutting operation can result in either a ZZ or an AM shaped edge. Consequently, there are four distinct types of nanoribbon configurations, as illustrated in Fig. 4, denoted as the SBC-ZZ edge, SBC-AM edge, WBC-ZZ edge, and WBC-AM edge, respectively.

To demonstrate the evolution of topological edge states across different phases in the present MKM model, we begin with an overview of topological edge states in the  $\mathbb{Z}_2$  TI zone. Figure 5 presents the full band structures of four types of nanoribbons with varying  $\eta$  and a fixed  $\lambda_R = 0$ . Focusing on the edge states, we make three key observations:

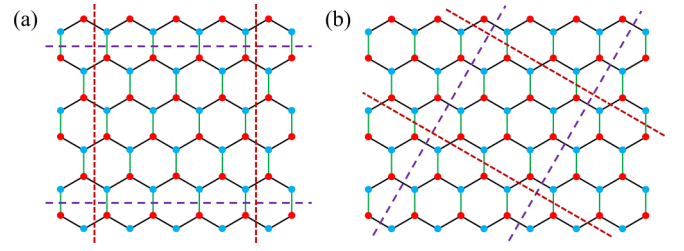


FIG. 4. Illustrations of zigzag (ZZ) and armchair (AM) edges. (a) Strong-bond-cutting (SBC)-ZZ (purple dashed line) and weak-bond-cutting (WBC)-AM (dark-red dotted line) edges. (b) WBC-ZZ (purple dashed line) and SBC-AM (dark-red dotted line) edges. Here, the green and black solid lines denote  $\eta t$  and  $t$  nearest-neighbor (NN) hoppings, respectively.

(i) In the  $\mathbb{Z}_2$  TI zone [Figs. 5(a1)–5(d1)], topological helical edge states are consistently observed. Specifically, at  $\eta = 1$ , the band structures replicate those of the  $\mathbb{Z}_2$  TI phase in the KM model [1]. According to Kane and Mele's argument [1], the crossings of two edge states at  $k = \pi$  for ZZ edges [Figs. 5(a1) and 5(b1)] or at  $k = 0$  for AM edges [Figs. 5(c1) and 5(d1)] form a Kramers doublet, which is robust against any TR-symmetric perturbations. (ii) In the SBC nanoribbons, edge states always emergence, as confirmed by Figs. 5(b1)–5(b4) for the SBC-ZZ edge and Figs. 5(d1)–5(d4) for the SBC-AM edge. This is due to the anisotropic NN hopping effect, which causes the Wannier centers to relocate at the strong bonds (green bars in Fig. 4), leading to the mismatches between lattice sites and Wannier centers [50]. This resembles the SSH model [49], in which the edge states emerge at cleavage terminations intersecting the Wannier centers. (iii) In the SOTI phase zone, as shown in Figs. 5(b3) and 5(d3), edge states are completely separated from the bulk bands. At  $-0.5 < \eta < 0.5$ , the edge states compress into a quasi-flat band in the middle of the bulk band gap, akin to the

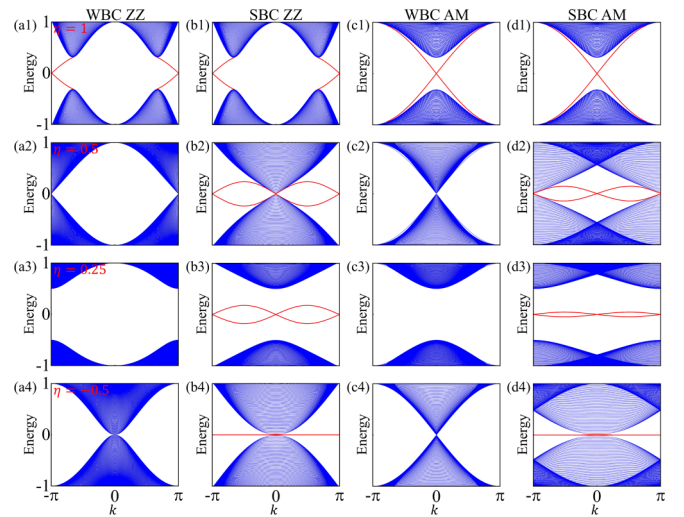


FIG. 5. Band structures of nanoribbons with (a) weak-bond-cutting (WBC)-zigzag (ZZ) edge, (b) strong-bond-cutting (SBC)-ZZ edge, (c) WBC-armchair (AM) edge and (d) SBC-AM edge. The Rashba spin-orbit coupling (RSOC) strengths are set to  $\lambda_R = 0$ . The in-gapped edge states are marked by red lines.

behaviors found in phosphorene [50,51] and the modified Haldane model [40].

### A. Edge states in SOTI phase

It should be emphasized that, in the SOTI phase, the edge states cross the Fermi energy an even number of times within the intervals  $k \in [0, \pi)$  or  $k \in [\pi, 2\pi)$ . As a result, these states contribute neither charge nor spin currents and do not support nonzero spin Hall conductivity [8]. Notably, these gapless edge states in the SOTI phase have been suggested to be  $\mathbb{Z}_2$  trivial, as they can be eliminated by pushing all the bound states out of the gap [3]. Even at the critical triple point  $T_2$ , the edge states that coexist with bulk states, as shown in Figs. 5(b2) and 5(d2), remain  $\mathbb{Z}_2$  trivial. In the weak bonding limit (i.e., small  $\eta$ ), these detached edge states resemble localized trap states that might be induced by the impurities deposited on the edge of the nanoribbon. Therefore, in both SBC or WBC nanoribbons, when the system transitions from the SOTI phase to the  $\mathbb{Z}_2$  TI phases at the critical point ( $\eta = 0.5$ ), the (topological) QPTs characterized by an even or odd number of Kramers pairs at the Fermi surface are still well defined by the  $\mathbb{Z}_2$  topological invariant. However, although these detached edge states are  $\mathbb{Z}_2$  trivial, their localized nature suggests a potential avenue for manipulating higher-order topological states that are more strongly localized in the finite-size systems [52]. We suggest that these localized edge states are a significant signature of the SOTI phase.

### B. Edge states in WM phases

In the WM phases, Fermi arc edge states are a universal feature across all types of nanoribbons. For example, in Fig. 6, the existence of these edge states is evident in the edge energy spectra of the nanoribbons across three WM phases. Like Fermi arc surface states in 3D WMs [30–33], the edge states in 2D WM phases bridge the projections of two WPs, thereby named Fermi arc edge states. Furthermore, these Fermi arc edge states exhibit double degeneracy that is protected by mirror symmetry and hence form closed loops, as depicted in Fig. 7.

In Fig. 7, we schematically illustrate the evolution of Fermi arc edge states through various phase transitions:  $\mathbb{Z}_2$  TI-WM<sub>2</sub>-WM<sub>3</sub>-WM<sub>1</sub>-SOTI-WM<sub>2</sub>, following the path indicated by the black dashed line in Fig. 2(a). The Fermi arc edge states are shown as arcs that connect the WPs. It is worth noting that, in each BZ, the red and blue arcs independently represent two distinct types of nanoribbons: SBC and WBC nanoribbons, respectively. The Fermi arc edge states evolved from the helical edge states of  $\mathbb{Z}_2$  TI phase first appear when the path C-D intersects the blue phase boundary, as shown in Fig. 7(a). At this critical phase transition condition, two pairs of Fermi arc edge states form a closed loop connecting two neutral WPs, distinguishing them topologically from the helical edge states in the  $\mathbb{Z}_2$  TI. As the system transforms into the WM<sub>2</sub> phase, each neutral degeneracy splits into two WPs of opposite chirality. As a result, the endpoints of the Fermi arc edge states must exhibit opposite chirality, maintaining a neutral total charge within each loop.

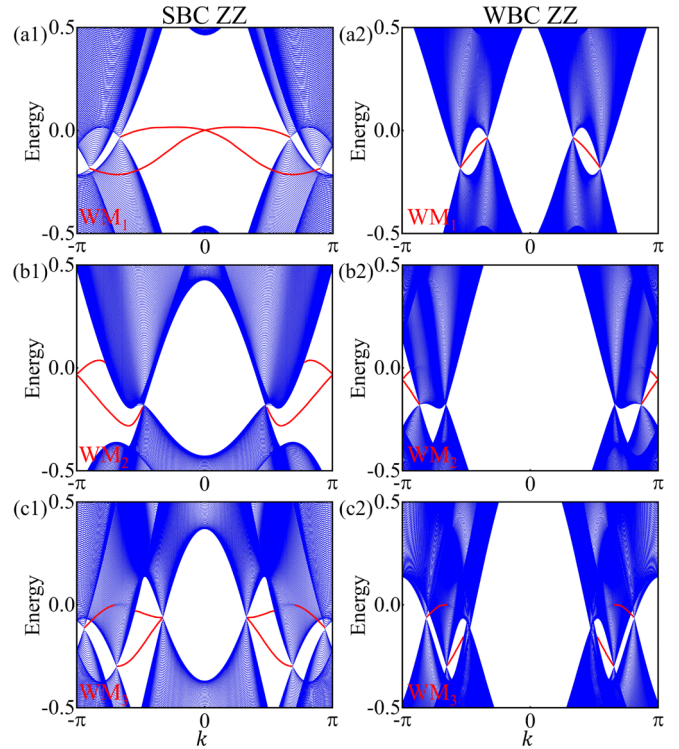


FIG. 6. Energy spectra of (1) strong-bond-cutting (SBC)-zigzag (ZZ) and (2) weak-bond-cutting (WBC)-ZZ nanoribbons in (a) WM<sub>1</sub>, (b) WM<sub>2</sub>, and (c) WM<sub>3</sub>. The corresponding parameters ( $\eta, \lambda_R/\lambda_{SO}$ ) in Weyl metal (WM) phase zones are marked as D–F in Fig. 2(a).

With the gap closing along the symmetry line  $K_1$ - $\Gamma$ - $K$  and the emergence of additional neutral degeneracies at the red phase boundary between WM<sub>2</sub> and WM<sub>3</sub>, a Fermi arc edge state arises in the SBC nanoribbon. As shown in Fig. 7(c), each new neutral degeneracy acts as an intermediate node, connecting the (red) Fermi arc edge states to a pair of WPs with opposite chirality. This results in the Fermi arc edge states forming two interconnected loops to ensure neutrality. In contrast, the (blue) Fermi arc edge states in the WBC nanoribbon maintain a single-loop structure, leaving the neutral degeneracies isolated. Upon crossing the red phase boundary, the neutral degeneracies further split, creating two extra pairs of WPs. In the WM<sub>3</sub> phase, as shown in Fig. 7(d), abundant Fermi arc edge states appear in both SBC and WBC nanoribbons, forming multiple independent loops connected to the WPs of opposite chirality. We suggest that the topological structure of the loops can be applied to characterize the topological QPTs among the WMs.

Similar patterns can be observed for the remaining path. For example, the role of neutral degeneracies as intermediate nodes is evident in Fig. 7(e), corresponding to the scenario at the gray boundary ( $\eta = 0.5$ ) in Fig. 2(a), where WM<sub>3</sub> transitions to the WM<sub>1</sub>. In WM<sub>1</sub>, the Fermi arc edge states, as shown in Fig. 7(f), replicate the behavior observed in WM<sub>2</sub> shown in Fig. 7(b). It is crucial to emphasize that the Fermi arc edge states solely connected to the neutral degeneracies shown in Figs. 7(a), 7(g), and 7(h) are fundamentally the same as the  $\mathbb{Z}_2$  trivial states that coexist with bulk states. As the system

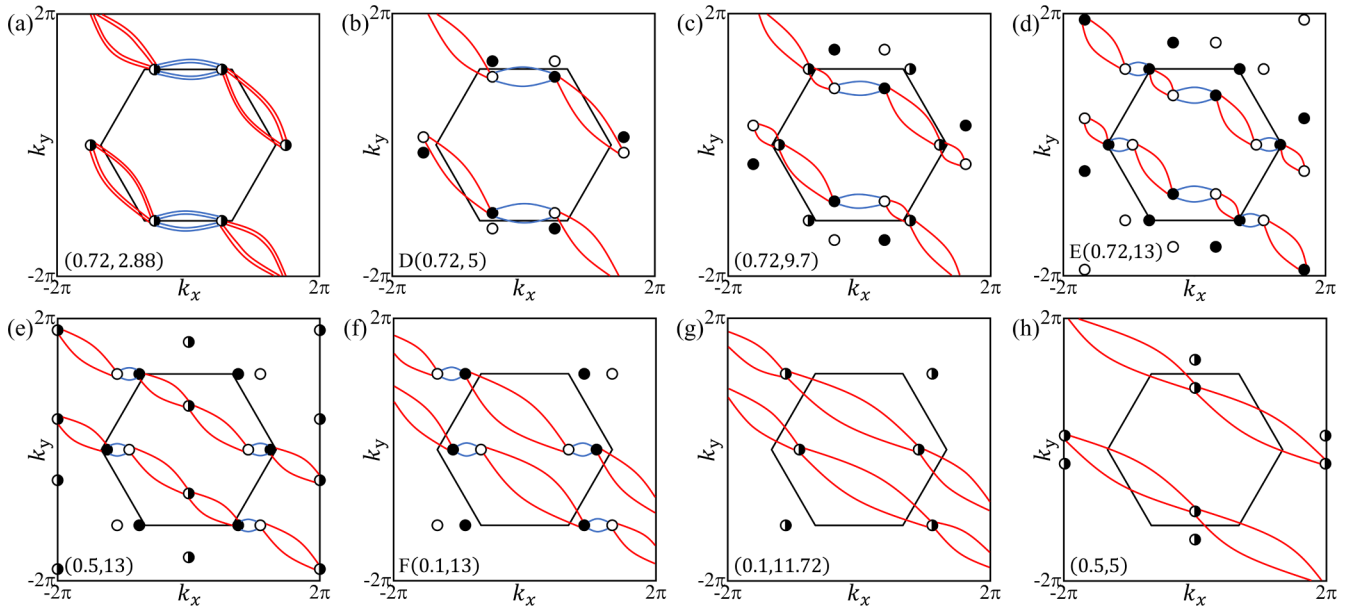


FIG. 7. Schematics depicting the evolution of Fermi arc edge states during quantum phase transitions (QPTs):  $\mathbb{Z}_2$  topological insulator (TI)-WM<sub>2</sub>-WM<sub>3</sub>-WM<sub>1</sub>-second-order TI (SOTI)-WM<sub>2</sub> following the path C → (b) D → (d) E → (f) F → G → C in Fig. 2(a). Panels (a), (c), (e), (g), and (h) correspond to the critical phase boundaries between the QPTs. Weyl points (WPs) with chirality  $-$  and  $+$  are represented by the black and white solid circles, respectively, while neutral degeneracies are marked by half white and half black circles. Red and blue arcs depict the Fermi arc edge states for strong-bond-cutting (SBC) and weak-bond-cutting (WBC) nanoribbons, respectively.

transitions to the SOTI phase, the neutral degeneracies are gapped out, and Fermi arc edge states detach from the bulk, finally forming localized edge states with in-gapped quasiflat band structures, as depicted in Figs. 5(b3) and 5(d3).

It is also important to emphasize that, in the 2D WM phases, the Fermi arc edge states are very fragile. For example, in contrast with the 3D Weyl nodes whose low-energy effective Hamiltonian contains all four Pauli matrices, the description of 2D WPs employs only two Pauli matrices, i.e.,  $\sigma_x$  and  $\sigma_y$  [34]. Consequently, additional perturbations or disorders proportional to  $\sigma_z$  will gap out the 2D WPs, leading to the breakdown of Fermi arc edge states. On the other hand, the introduction of magnetic impurities also leads to backscattering at the edge states [53], resulting in the destruction of the edge ballistic transportation. Nevertheless, due to the spin-momentum locking enforced by TR symmetry, the Fermi arc edge states in the 2D WM phases can resist weak nonmagnetic disorders [53].

#### IV. CORNER STATES IN THE MKM MODEL

In this section, we demonstrate the realization of corner states in the SOTI phase using a rhombus-shaped nanodisk. The rhombus-shaped nanodisk tailed off a honeycomb lattice is depicted in Fig. 8(a). The size of the nanodisk, denoted as  $L$ , is determined by the number of benzene rings along its edge. Figure 8(b) displays the energy spectrum for a rhombus-shaped nanodisk of size  $L = 15$ , under the phase parameters (0.1, 0). Here, four zero-energy in-gapped states are highlighted with blue and red solid circles, signifying the emergence of quantized charge states. The inset of this figure further corroborates the localizations of the filled corner

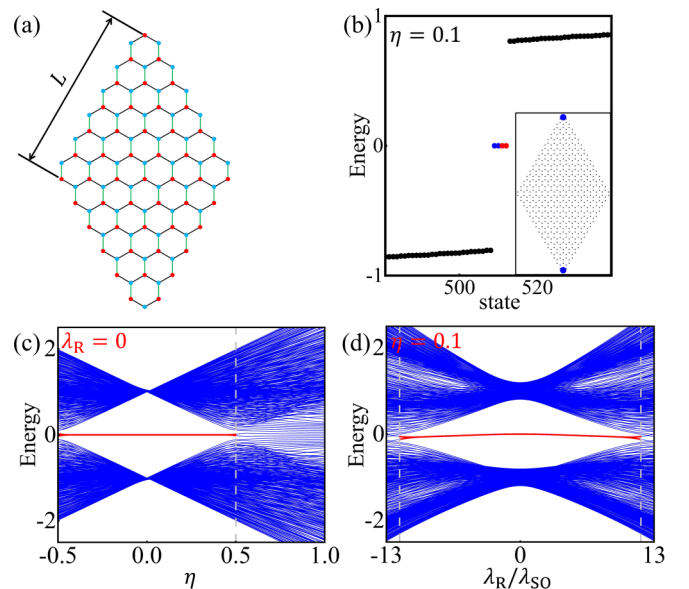


FIG. 8. Corner states in the modified Kane-Mele (MKM) model. (a) Illustration of a rhombus-shaped nanodisk of size  $L = 6$ , with green and black solid lines indicating  $\eta t$  and  $t$  nearest-neighbor (NN) hoppings, respectively. (b) Energy spectrum for  $\eta = 0.1$  and  $\lambda_R = 0$ , highlighting corner states in red and blue circles. The inset displays the probability distribution of the states labeled by blue circles. (c) Energy spectrum variation with the anisotropic parameter  $\eta$  at  $\lambda_R = 0$ . (d) Energy spectrum response to varying Rashba spin-orbit coupling (RSOC) strength at  $\eta = 0.1$ . In panels (b)–(d), the size of the nanodisk is chosen as  $L = 15$ . Corner states are marked in red in (b) and (d).



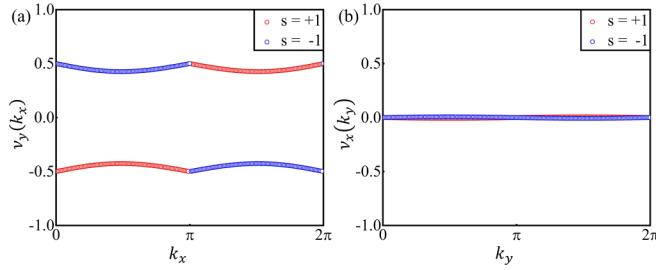


FIG. 9. Wannier bands along (a)  $k_x$  and (b)  $k_y$  for  $s = +1$  (red empty circle) and  $s = -1$  (blue empty circle). The anisotropic parameter is chosen as  $\eta = 0.1$ .

states (marked in blue) at the top and bottom lattice sites. To further validate the second-order topology in the SOTI phase, we plot the energy spectrum as a function of the anisotropic parameters  $\eta$ , while sweeping across the  $\lambda_R/\lambda_{SO}$  axis. As an example, Fig. 8(c) demonstrates the persistence of in-gapped corner states, represented by the red lines, within the range of  $-0.5 < \eta < 0.5$  at  $\lambda_R = 0$ .

To capture the characters of the localized states, the Bloch wave functions are projected onto the Wannier representation. Consequently, the nontrivial topology of a SOTI can be captured by the polarization of occupied bands, which is formulated as [10,11]

$$p_\alpha = \frac{1}{N_\beta} \sum_{k_\beta} \sum_{j=1}^{N_{occ}} v_\alpha^j(k_\beta), \quad (10)$$

where  $\alpha, \beta = x, y$ , with  $\alpha \neq \beta$ ,  $N_\beta$ , is the number of lattice sites along  $\beta$ , and  $v_\alpha^j(k_\beta)$  refers to the  $j$ th Wannier band. For the sake of simplicity but without loss of generality, we initially set  $\lambda_R = 0$ . It will be discussed later that the higher-order bulk-boundary correspondence is maintained up to a critical  $\lambda_R$ . In the presence of inversion symmetry, the Hamiltonian in Eq. (2) can be decoupled into two independent parts [54]:

$$H_s(\mathbf{k}) = d_1(\mathbf{k})\sigma_x - d_{12}(\mathbf{k})\sigma_y + sd_{15}(\mathbf{k})\sigma_z, \quad (11)$$

with  $s = \pm 1$  representing the spin index. The mirror symmetry along  $\alpha$  imposes a restriction on the allowable Wannier bands [10,11]:  $v_\alpha^j(k_\beta) \stackrel{M_\alpha}{=} -v_\alpha^j(k_\beta)$ . Due to the gauge invariance,  $p_\alpha$  is defined modulo 1. Therefore,  $p_\alpha$  is quantized and takes values of either 0 or  $\frac{1}{2}$ . Figure 9 illustrates the Wannier bands for (a)  $v_y^s(k_x)$  and (b)  $v_x^s(k_y)$ , respectively. It is readily apparent that the Wannier band  $v_y^s(k_x)$  localizes  $\sim \frac{1}{2}$ , as shown in Fig. 9(a), while  $v_x^s(k_y)$  is essentially zero, as depicted in Fig. 9(b). Consequently, these unique Wannier bands give rise to an anisotropic polarization,  $(p_x^s, p_y^s) = (0, \frac{1}{2})$ , which indicates that the electrons are localized at the center of the strong bond. This observation is consistent with those in the modified honeycomb lattice [50] and the modified Haldane model [40].

In the nanodisk configuration, a total of  $2L(L+2)$  bands is occupied by electrons at half-filling. However, due to the anisotropic polarization in the Wannier configuration,  $2L(L+2) - 2$  bulk electrons are moved to the center of the strong bond. This movement aligns them with the

positive ionic centers, manifesting as the dipoles or multipoles in the bulk. Consequently, there are two lonely electrons that must be positioned at the corners to maintain the charge neutrality of the system. Owing to the  $C_{2z}$  symmetry in the absence of staggered on-site potential, these two electrons are localized at the corners where two ZZ edges intersect. Indeed, in the limit of  $\lambda_R = 0$ , the charge-localized density can also be deduced by superimposing two modified Haldane models, where each contributes  $\frac{1}{2}$  electron at two corners [40]. This observation aligns with the spirit of Eq. (11) and the fact that the KM model can be decoupled into two Haldane models with opposite flux.

Finally, we briefly discuss the impact of RSOC ( $\lambda_R \neq 0$ ) on the corner states. As depicted in the energy spectrum in Fig. 9(d), an increase in RSOC eventually leads to elimination of corner states, accompanied with a QPT to the  $WM_1$  phase. The introduction of RSOC breaks both particle-hole symmetry and inversion symmetry, destabilizing the in-gapped corner states from their zero-energy positions as the bulk gap narrows. In simpler terms, NN RSOC imposes a strong connection between the two corner-localized electrons and their nearest bulk electrons. At a critical RSOC strength where the bulk gap closes, the corner states are absorbed into the bulk, as shown in Fig. 9(d).

## V. CONCLUSIONS

In summary, we have established a generalized phase diagram in the parameter space ( $\eta, \lambda_R/\lambda_{SO}$ ) to demonstrate QPTs in the MKM model with  $C_{3z}$  symmetry broken by anisotropic NN hopping but  $C_{2z}$  symmetry retained by removing the staggered on-site potential. The presence of  $C_{2z}$  symmetry can induce a filling anomaly in a strategically designed Wannier configuration within a certain parameter scale, which opens an active avenue to realize second-order topological corner states. The incorporated anisotropic NN hopping and RSOC break the  $C_{3z}$  and inversion symmetries, and thereby, tuning the parameters leads to QPTs among  $\mathbb{Z}_2$  TI,  $\mathcal{P}$ -breaking 2D WM, and SOTI phases. Notably, the SOTI and  $\mathbb{Z}_2$  TI phases persist even when the inversion symmetry is broken. The  $\mathcal{P}$ -breaking 2D WM phases occur at the critical RSOC, where the bulk band gap closes as the insulating phases undergo the QPTs at the phase boundaries delineated by Eqs. (6) and (7).

We also demonstrated that the interplay between anisotropy and RSOC gives rise to three distinct types of  $\mathcal{P}$ -breaking 2D WM phases, each featured by 2D WPs with  $\pm 1$  topological charge and Fermi arc edge states. The creation and annihilation of neutral degeneracies play a crucial role in affecting the topological nature of the edge states during QPTs between insulating phases and WM phases. As the QPTs occur among the topological phases, we identified helical edge states, localized edge states with a quasiflat band structure, and Fermi arc edge states in the nanoribbon geometry. Finally, we theoretically demonstrated the realization of a SOTI phase in a rhombus-shaped nanodisk. Two corner states, each with an integer charge, emerge as the consequence of the filling anomaly between the



Wannier centers and the bulk atoms. These higher-order topological states, adhering to higher-order bulk-boundary correspondences, are characterized by a quantized anisotropic polarization which is protected by mirror symmetry.

## ACKNOWLEDGMENTS

This paper was supported by the Natural Science Foundation of Hunan Province, China (Grant No. 2023JJ30114).

- 
- [1] C. L. Kane and E. J. Mele, Quantum spin Hall effect in graphene, *Phys. Rev. Lett.* **95**, 226801 (2005).
- [2] C. L. Kane and E. J. Mele,  $\mathbb{Z}_2$  topological order and the quantum spin Hall effect, *Phys. Rev. Lett.* **95**, 146802 (2005).
- [3] M. Z. Hasan and C. L. Kane, Colloquium: Topological insulators, *Rev. Mod. Phys.* **82**, 3045 (2010).
- [4] X.-L. Qi and S.-C. Zhang, Topological insulators and superconductors, *Rev. Mod. Phys.* **83**, 1057 (2011).
- [5] C.-K. Chiu, J. C. Y. Teo, A. P. Schnyder, and S. Ryu, Classification of topological quantum matter with symmetries, *Rev. Mod. Phys.* **88**, 035005 (2016).
- [6] C. Wu, B. A. Bernevig, and S.-C. Zhang, Helical liquid and the edge of quantum spin Hall systems, *Phys. Rev. Lett.* **96**, 106401 (2006).
- [7] C. Xu and J. E. Moore, Stability of the quantum spin Hall effect: Effects of interactions, disorder, and  $\mathbb{Z}_2$  topology, *Phys. Rev. B* **73**, 045322 (2006).
- [8] S. Mondal and S. Basu, Vanishing of the quantum spin Hall phase in a semi-Dirac Kane-Mele model, *Phys. Rev. B* **105**, 235409 (2022).
- [9] M. Geier, L. Trifunovic, M. Hoskam, and P. W. Brouwer, Second-order topological insulators and superconductors with an order-two crystalline symmetry, *Phys. Rev. B* **97**, 205135 (2018).
- [10] W. A. Benalcazar, B. A. Bernevig, and T. L. Hughes, Quantized electric multipole insulators, *Science* **357**, 61 (2017).
- [11] W. A. Benalcazar, B. A. Bernevig, and T. L. Hughes, Electric multipole moments, topological multipole moment pumping, and chiral hinge states in crystalline insulators, *Phys. Rev. B* **96**, 245115 (2017).
- [12] L. Trifunovic and P. W. Brouwer, Higher-order bulk-boundary correspondence for topological crystalline phases, *Phys. Rev. X* **9**, 011012 (2019).
- [13] M. Ezawa, Edge-corner correspondence: Boundary-obstructed topological phases with chiral symmetry, *Phys. Rev. B* **102**, 121405(R) (2020).
- [14] B. Xie, H.-X. Wang, X. Zhang, P. Zhan, J.-H. Jiang, M. Lu, and Y. Chen, Higher-order band topology, *Nat. Rev. Phys.* **3**, 520 (2021).
- [15] Y. Ren, Z. Qiao, and Q. Niu, Engineering corner states from two-dimensional topological insulators, *Phys. Rev. Lett.* **124**, 166804 (2020).
- [16] C. Chen, Z. Song, J.-Z. Zhao, Z. Chen, Z.-M. Yu, X.-L. Sheng, and S. A. Yang, Universal approach to magnetic second-order topological insulator, *Phys. Rev. Lett.* **125**, 056402 (2020).
- [17] C.-M. Miao, Q.-F. Sun, and Y.-T. Zhang, Second-order topological corner states in zigzag graphene nanoflake with different types of edge magnetic configurations, *Phys. Rev. B* **106**, 165422 (2022).
- [18] D. Zhu, M. Kheirkhah, and Z. Yan, Sublattice-enriched tunability of bound states in second-order topological insulators and superconductors, *Phys. Rev. B* **107**, 085407 (2023).
- [19] B. Wang, Y.-C. Hung, X. Zhou, A. Bansil, and H. Lin, Higher-order topological phases hidden in quantum spin Hall insulators, *Phys. Rev. B* **108**, 245103 (2023).
- [20] W. A. Benalcazar, T. Li, and T. L. Hughes, Quantization of fractional corner charge in  $C_n$ -symmetric higher-order topological crystalline insulators, *Phys. Rev. B* **99**, 245151 (2019).
- [21] Y. Fang and J. Cano, Filling anomaly for general two- and three-dimensional  $C_4$  symmetric lattices, *Phys. Rev. B* **103**, 165109 (2021).
- [22] R. Takahashi, T. Zhang, and S. Murakami, General corner charge formula in two-dimensional  $C_n$ -symmetric higher-order topological insulators, *Phys. Rev. B* **103**, 205123 (2021).
- [23] H. Araki, T. Mizoguchi, and Y. Hatsugai, Phase diagram of a disordered higher-order topological insulator: A machine learning study, *Phys. Rev. B* **99**, 085406 (2019).
- [24] A. Agarwala, V. Juričić, and B. Roy, Higher-order topological insulators in amorphous solids, *Phys. Rev. Res.* **2**, 012067(R) (2020).
- [25] C.-A. Li, B. Fu, Z.-A. Hu, J. Li, and S.-Q. Shen, Topological phase transitions in disordered electric quadrupole insulators, *Phys. Rev. Lett.* **125**, 166801 (2020).
- [26] Z.-D. Song, B. Lian, R. Queiroz, R. Ilan, B. A. Bernevig, and A. Stern, Delocalization transition of a disordered axion insulator, *Phys. Rev. Lett.* **127**, 016602 (2021).
- [27] C. Lu, Z.-F. Cai, M. Zhang, H. Wang, Q. Ai, and T. Liu, Effects of disorder on Thouless pumping in higher-order topological insulators, *Phys. Rev. B* **107**, 165403 (2023).
- [28] B. Bradlyn, L. Elcoro, J. Cano, M. G. Vergniory, Z. Wang, C. Felser, M. I. Aroyo, and B. A. Bernevig, Topological quantum chemistry, *Nature (London)* **547**, 298 (2017).
- [29] T. Du, Y.-X. Li, H.-L. Lu, H. Zhang, and S. Du, The competition between the intrinsic and Rashba spin-orbit coupling and effects of correlations on Rashba SOC-driven transitions in the Kane-Mele model, *J. Phys.: Condens. Matter* **32**, 505601 (2020).
- [30] G. Xu, H. Weng, Z. Wang, X. Dai, and Z. Fang, Chern semimetal and the quantized anomalous Hall effect in  $\text{HgCr}_2\text{Se}_4$ , *Phys. Rev. Lett.* **107**, 186806 (2011).
- [31] X. Wan, A. M. Turner, A. Vishwanath, and S. Y. Savrasov, Topological semimetal and Fermi-arc surface states in the electronic structure of pyrochlore iridates, *Phys. Rev. B* **83**, 205101 (2011).
- [32] L. Balents, Weyl electrons kiss, *Physics* **4**, 36 (2011).
- [33] B. Q. Lv, T. Qian, and H. Ding, Experimental perspective on three-dimensional topological semimetals, *Rev. Mod. Phys.* **93**, 025002 (2021).
- [34] J.-Y. You, C. Chen, Z. Zhang, X.-L. Sheng, S. A. Yang, and G. Su, Two-dimensional Weyl half-semimetal and tunable quantum anomalous Hall effect, *Phys. Rev. B* **100**, 064408 (2019).
- [35] L. Jin, L. Wang, X. Zhang, Y. Liu, X. Dai, H. Gao, and G. Liu, Fully spin-polarized Weyl fermions and in/out-of-plane quantum anomalous Hall effects in a two-dimensional  $d^0$  ferromagnet, *Nanoscale* **13**, 5901 (2021).

- [36] H. Huan, Y. Xue, B. Zhao, H. Bao, L. Liu, and Z. Yang, Tunable Weyl half-semimetals in two-dimensional iron-based materials  $M\text{FeSe}$  ( $M = \text{Ti, In, Ga}$ ), *Phys. Rev. B* **106**, 125404 (2022).
- [37] Y. Yu, X. Xie, X. Liu, J. Li, F. M. Peeters, and L. Li, Two-dimensional semimetal states in transition metal trichlorides: A first-principles study, *Appl. Phys. Lett.* **121**, 112405 (2022).
- [38] P. R. Wallace, The band theory of graphite, *Phys. Rev.* **71**, 622 (1947).
- [39] S. M. Young and C. L. Kane, Dirac semimetals in two dimensions, *Phys. Rev. Lett.* **115**, 126803 (2015).
- [40] B. Wang, X. Zhou, H. Lin, and A. Bansil, Higher-order topological insulator phase in a modified Haldane model, *Phys. Rev. B* **104**, L121108 (2021).
- [41] Y. A. Bychkov and E. I. Rashba, Properties of a 2D electron gas with lifted spectral degeneracy, *Pis'ma Zh. Eksp. Teor. Fiz.* **39**, 66 (1984) [*JETP Lett.* **39**, 78 (1984)].
- [42] A. Varykhalov, J. Sánchez-Barriga, A. M. Shikin, C. Biswas, E. Vescovo, A. Rybkin, D. Marchenko, and O. Rader, Electronic and magnetic properties of quasifreestanding graphene on Ni, *Phys. Rev. Lett.* **101**, 157601 (2008).
- [43] G. Frank, G. Pintér, and A. Pályi, Singularity theory of Weyl-point creation and annihilation, [arXiv:2309.05506](https://arxiv.org/abs/2309.05506).
- [44] L. Lu, L. Fu, J. D. Joannopoulos, and M. Soljačić, Weyl points and line nodes in gyroid photonic crystals, *Nat. Photon.* **7**, 294 (2013).
- [45] J.-M. Hou and W. Chen, Weyl semimetals in optical lattices: Moving and merging of Weyl points, and hidden symmetry at Weyl points, *Sci. Rep.* **6**, 33512 (2016).
- [46] Y. Guo, Z. Lin, J.-Q. Zhao, J. Lou, and Y. Chen, Two-dimensional tunable Dirac/Weyl semimetal in non-Abelian gauge field, *Sci. Rep.* **9**, 18516 (2019).
- [47] S. M. Young, S. Zaheer, J. C. Y. Teo, C. L. Kane, E. J. Mele, and A. M. Rappe, Dirac semimetal in three dimensions, *Phys. Rev. Lett.* **108**, 140405 (2012).
- [48] H. B. Nielsen and M. Ninomiya, The Adler-Bell-Jackiw anomaly and Weyl fermions in a crystal, *Phys. Lett. B* **130**, 389 (1983).
- [49] W. P. Su, J. R. Schrieffer, and A. J. Heeger, Solitons in polyacetylene, *Phys. Rev. Lett.* **42**, 1698 (1979).
- [50] M. Ezawa, Minimal models for Wannier-type higher-order topological insulators and phosphorene, *Phys. Rev. B* **98**, 045125 (2018).
- [51] M. M. Grujić, M. Ezawa, M. Ž. Tadić, and F. M. Peeters, Tunable skewed edges in puckered structures, *Phys. Rev. B* **93**, 245413 (2016).
- [52] L. Wang, Y. Jiang, J. Liu, S. Zhang, J. Li, P. Liu, Y. Sun, H. Weng, and X.-Q. Chen, Two-dimensional obstructed atomic insulators with fractional corner charge in the  $MA_2Z_4$  family, *Phys. Rev. B* **106**, 155144 (2022).
- [53] J. D. Mella and L. E. F. F. Torres, Robustness of spin-polarized edge states in a two-dimensional topological semimetal without inversion symmetry, *Phys. Rev. B* **105**, 075403 (2022).
- [54] D. N. Sheng, Z. Y. Weng, L. Sheng, and F. D. M. Haldane, Quantum spin-Hall effect and topologically invariant Chern numbers, *Phys. Rev. Lett.* **97**, 036808 (2006).